Supporting Information

Study of Structural and Composition Redesign to Enhanced the Thermostability and Electrochemical Performance of Co-less Ni-rich $LiNi_{0.92}Co_{0.04}Mn_{0.04}O_2$ Layered Cathode through Transition-metal Concentration Gradient Strategies

Yola Bertilsya Hendri[a], Manojkumar Seenivasan[a], Juliya Jeyakumar[a], Yi-Shiuan Wu[a], She-Huang Wu[a,c], Jeng-Kuei Chang[d], Amun Amri[f], Rajan Jose[a,e], Chun-Chen Yang[a,b,g]*

[a]*Battery Research Center of Green Energy, Ming Chi University of Technology, Taishan, New Taipei City, 24301, Taiwan*

[b]*Department of Chemical Engineering, Ming Chi University of Technology, Taishan, New Taipei City, 24301, Taiwan*

[c]*Graduate Institute of Science and Technology, National Taiwan University of Science and Technology, 43, Sec. 4, Keelung Road, Taipei 106, Taiwan*

[d]*Department of Materials Science and Engineering, National Yang Ming Chiao Tung University, 1001 University Road, Hsinchu, 30010, Taiwan*

[e]*Nanostructured Renewable Energy Materials Laboratory, Faculty of Industrial Sciences and Technology, University Malaysia Pahang, 26300 Kuantan, Malaysia*

[f]*Department of Chemical Engineering, University of Riau, Panam, Pekanbaru, 28293, Indonesia*

[g]*Department of Chemical and Materials Engineering, and Green Technology Research Center, Chang Gung University, Taoyuan City 333, Taiwan*

*Corresponding author. Tel.: +886 2 29089899 ext.4962/4952;

fax: +886 2 29085941.

E-mail: ccyang@mail.mcut.edu.tw (C.-C. Yang)

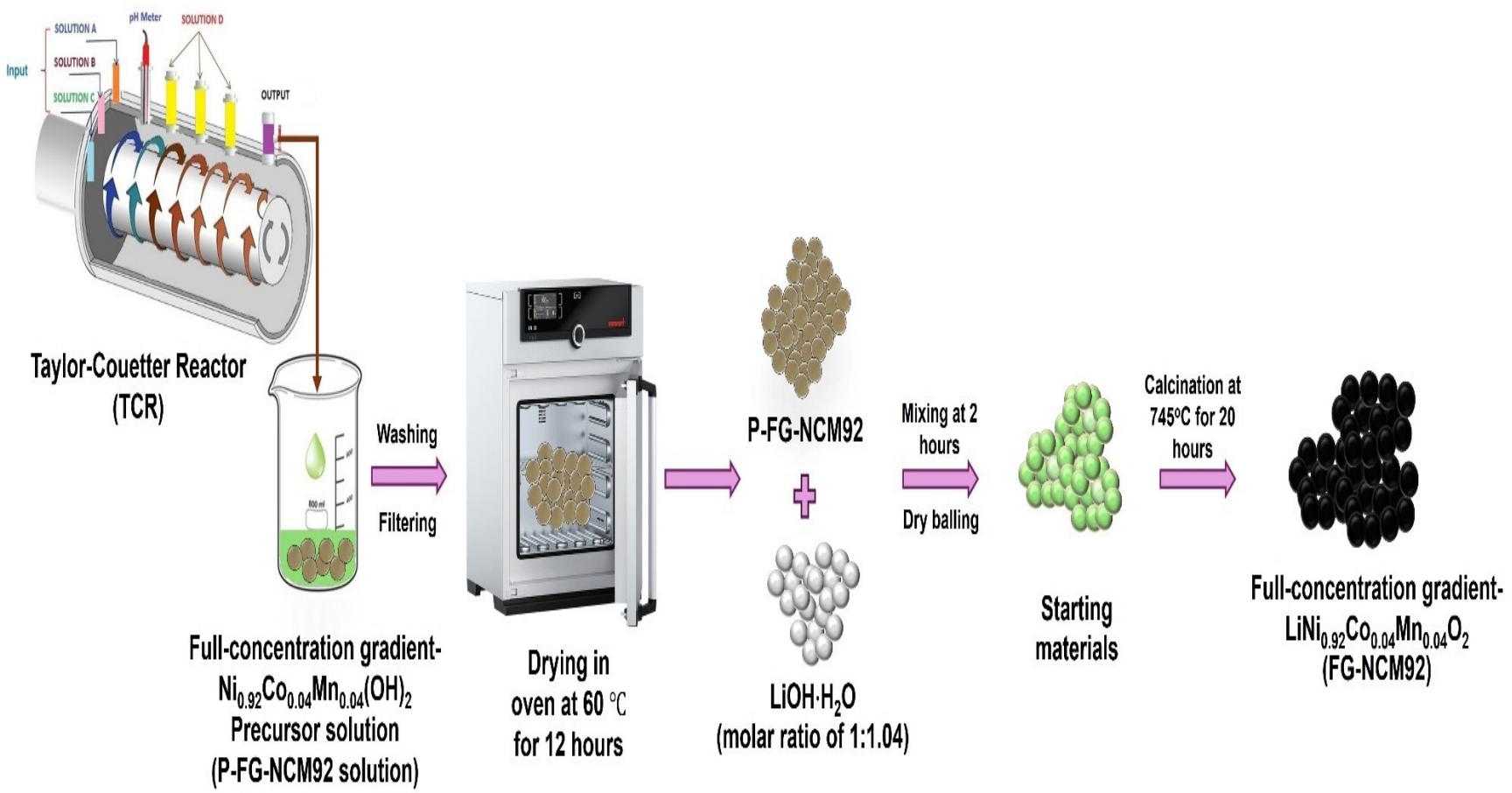

Fig. S1. Schematic diagram of FG-NCM92 synthesis process by using a novel scalable Taylor–Vortex Reactor (TVR).

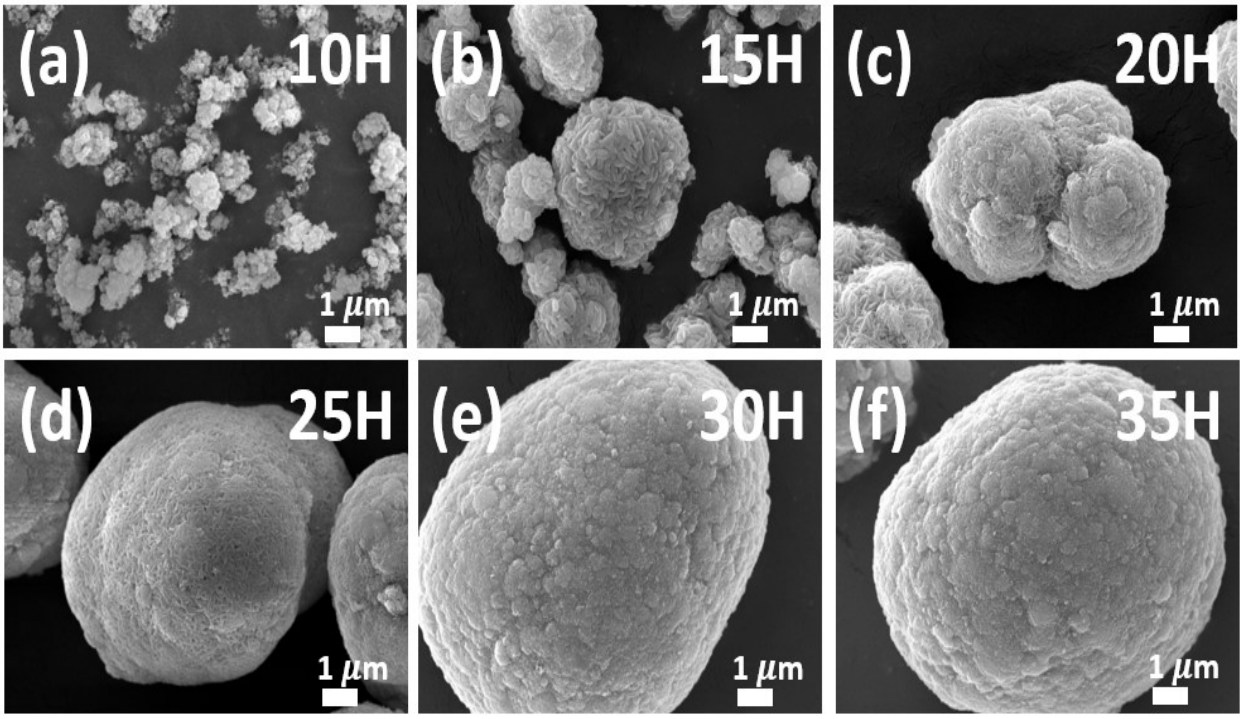

Fig. S2. The morphological evolution of P-FG-NCM92 hydroxide particles as a function of reaction time synthesis by using a novel scalable Taylor–Vortex Reactor (TVR): (a). 10 h, (b). 15 h, (c). 20 h, (d). 25 h, (e). 30 h, (f). 35 h, respectively.

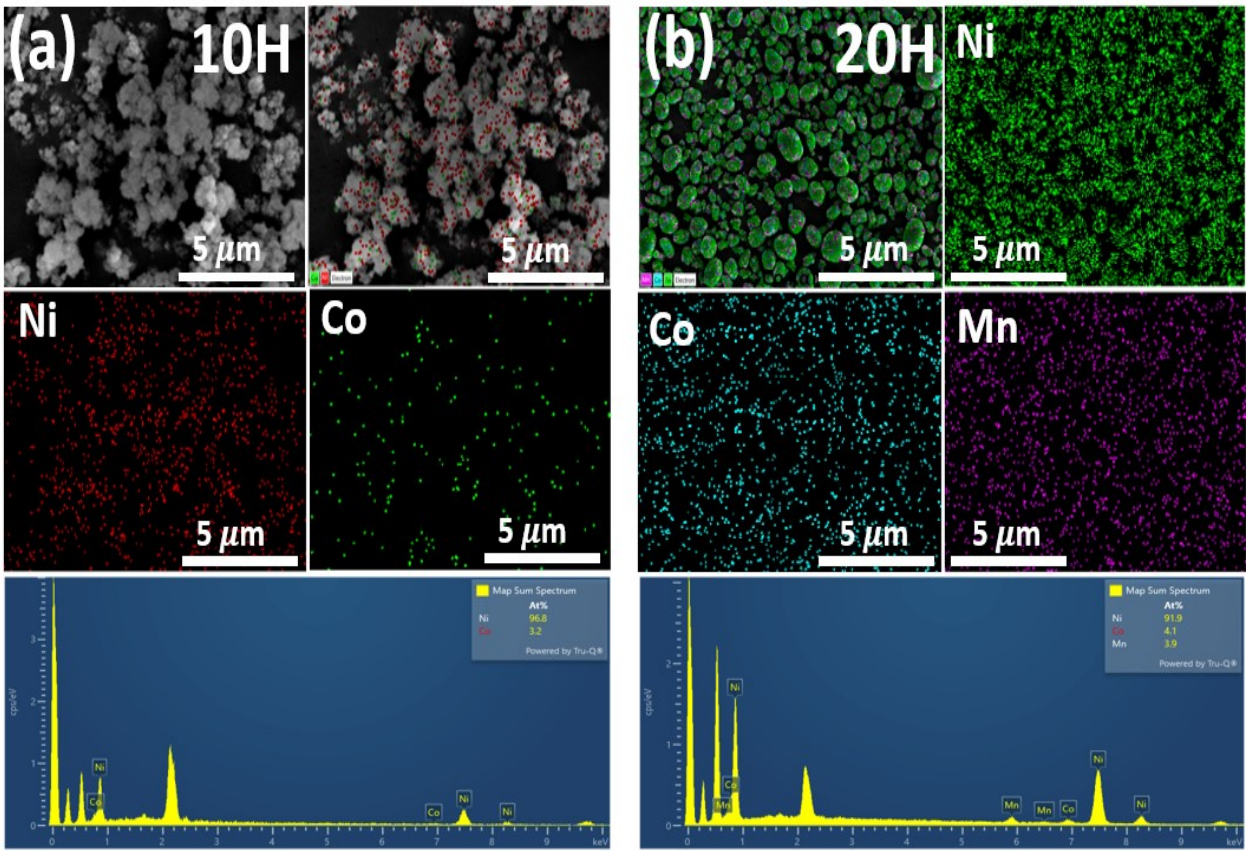

Fig. S3. EDX images of FG-$Ni_{0.92}Co_{0.04}Mn_{0.04}(OH)_2$ precursors synthesized by using TVR reactor at (a) 10 h, and (b) 20 h.

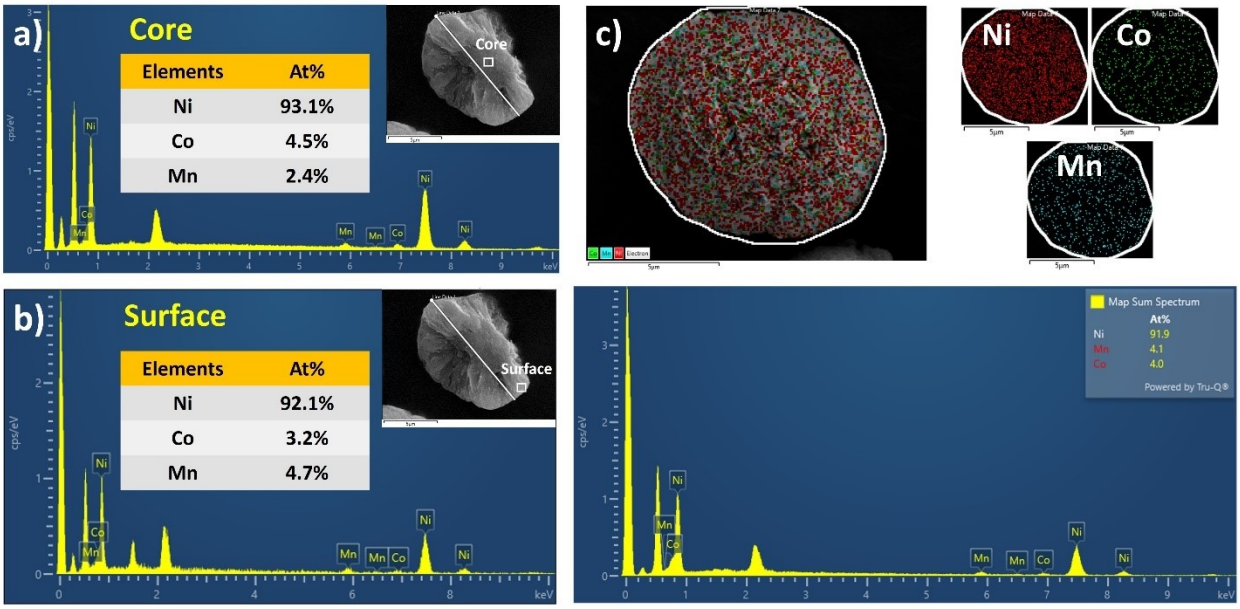

Fig. S4. The EDS graph of (a) area core and (b) area surface in the FG-$Ni_{0.92}Co_{0.04}Mn_{0.04}(OH)_2$, and (c) single particle of FG-$Ni_{0.92}Co_{0.04}Mn_{0.04}(OH)_2$.

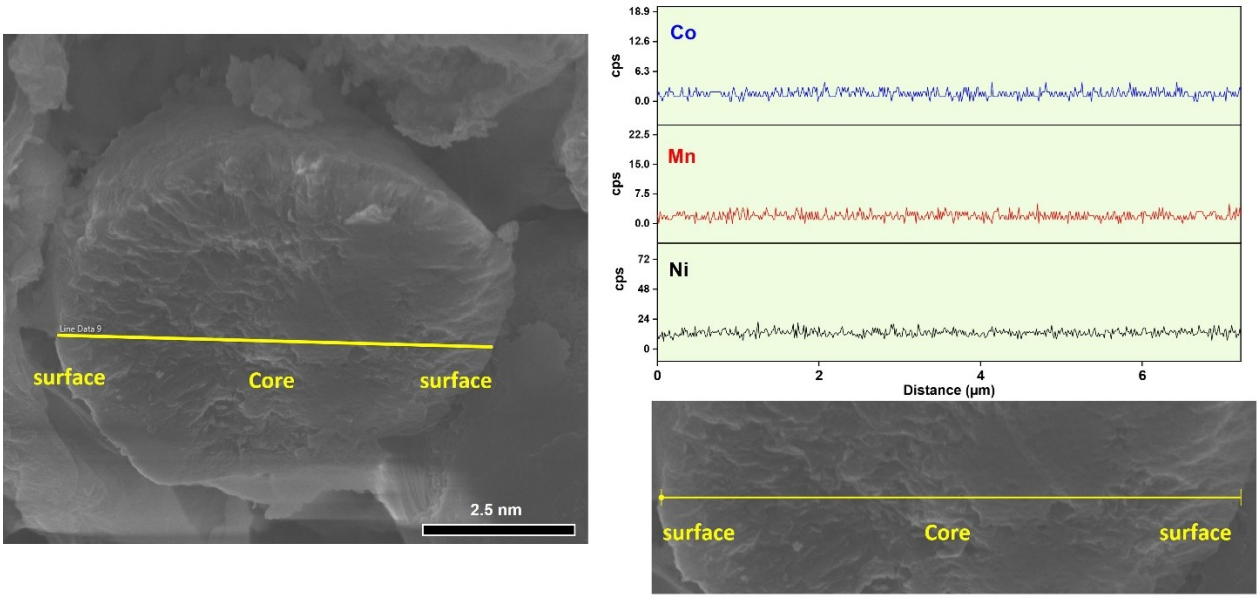

Fig. S5. FESEM-EDS-line-scanning of Ni, Co, Mn for P-NG-NCM92 precursors synthesized by a Taylor-Vortex Reactor (TVR).

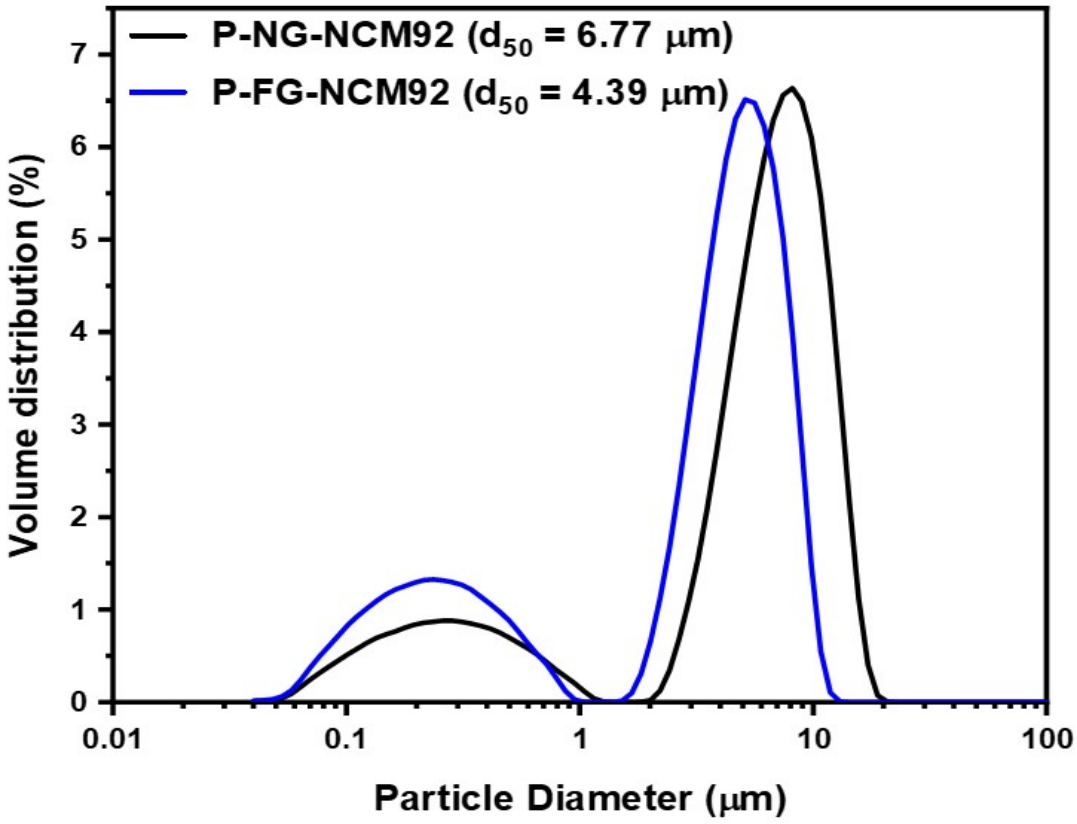

Fig. S6. Particle size distribution of (a) P-NG-NCM92 (black line), and (b) P-FG-NCM92 (blue line) hydroxide precursors.

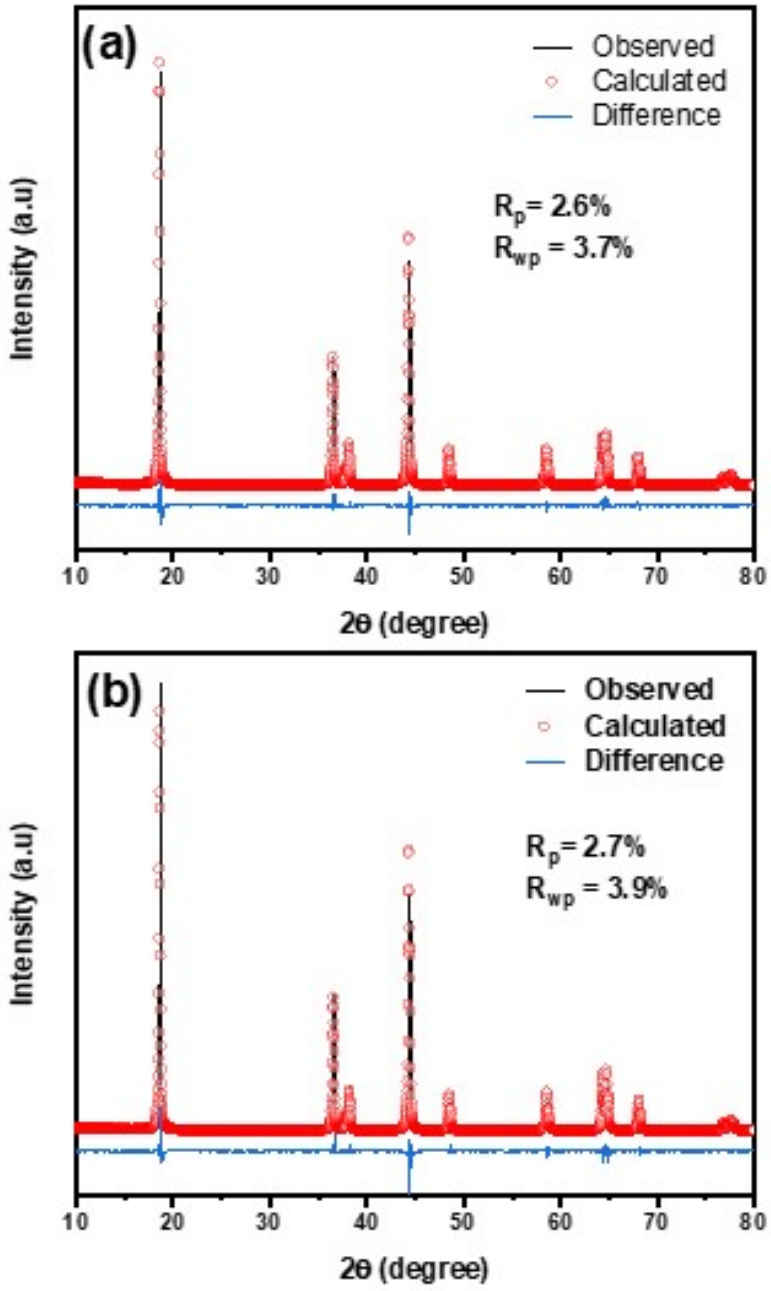

Fig. S7. XRD Rietveld refinement results of (a) NG-NCM92, and (b) FG-NCM92 layered oxides cathode materials, respectively.

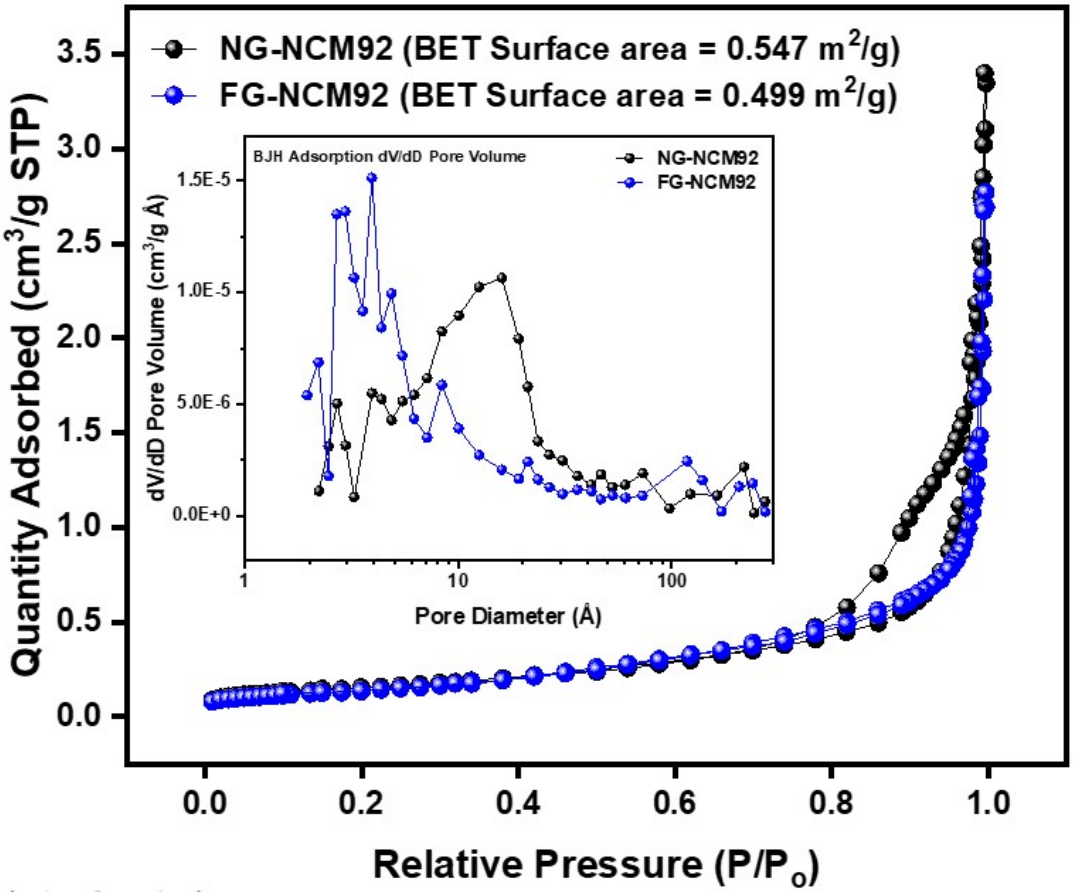

Fig. S8. BET specific surface area and pore size distribution (shown in the inset) of NG-NCM92 and FG-NCM92 layered oxide cathode materials.

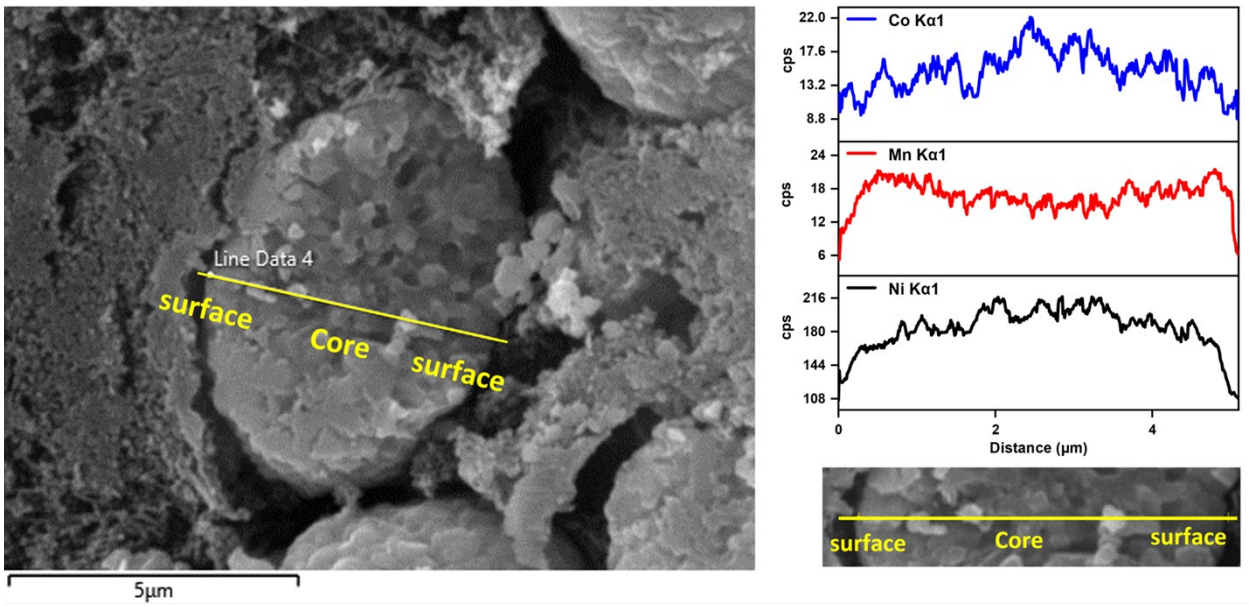

Fig. S9. SEM-EDS-line-scanning of Ni, Co, Mn for FG-NCM92 cathode.

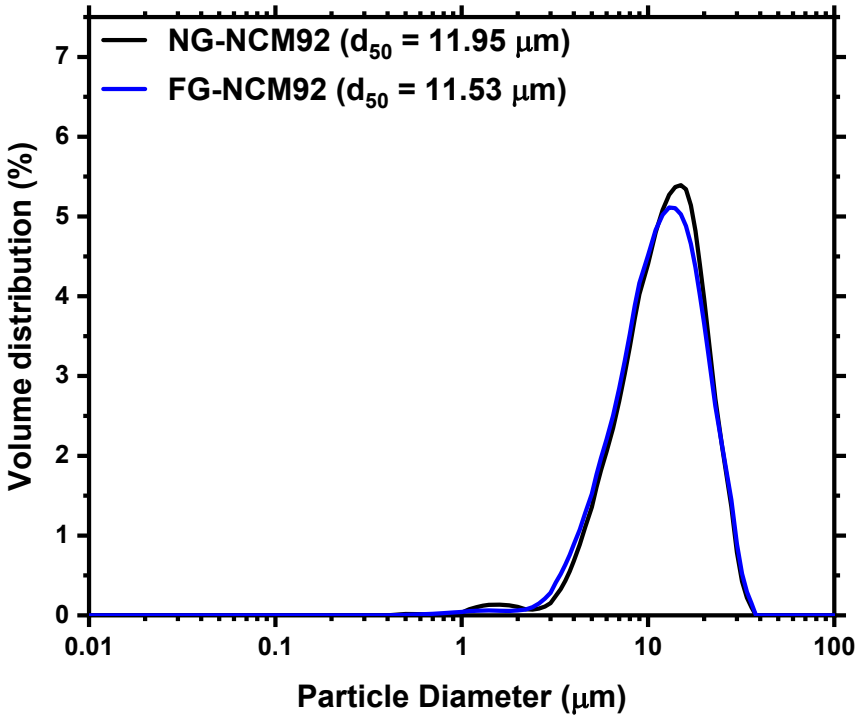

Fig. S10. Particle size distribution of NG-NCM92 (black line) and FG-NCM92 (blue line) cathode oxide materials.

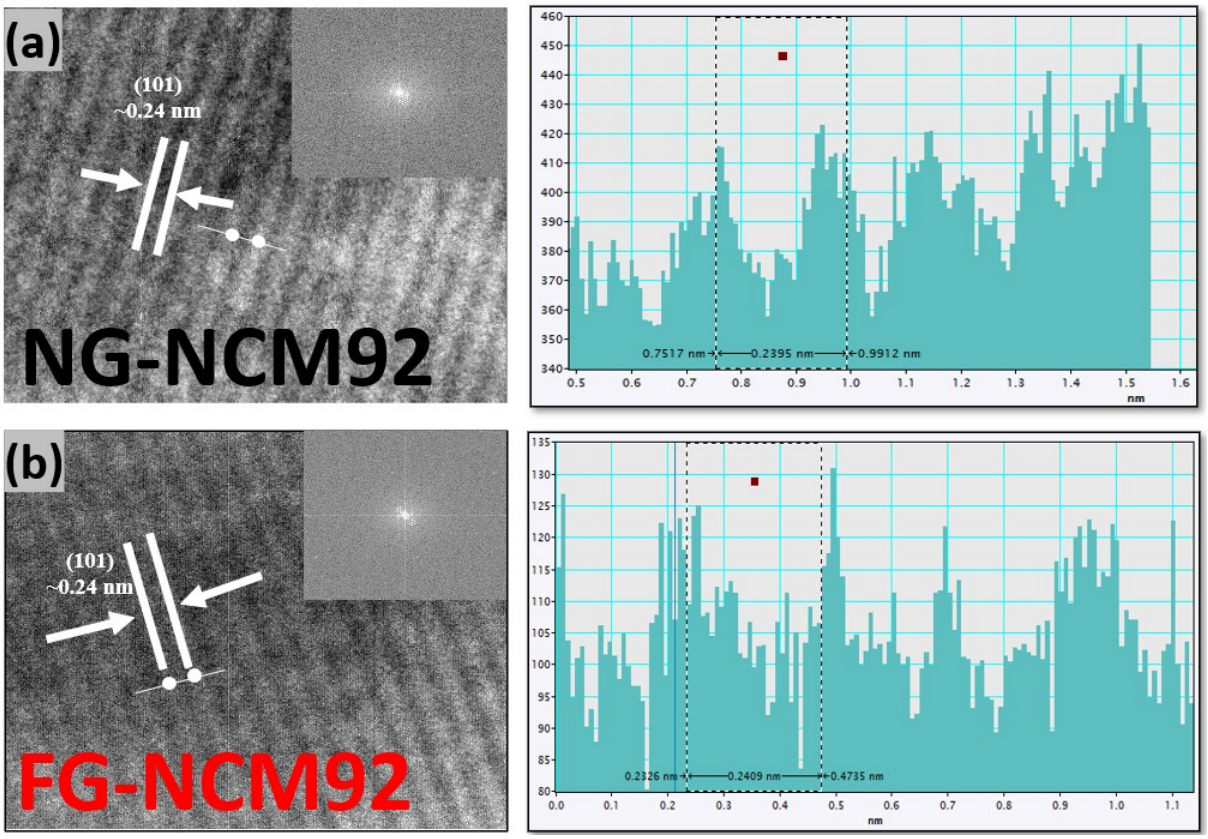

Fig. S11. The FFT and IFFT analysis of (a) NG-NCM92, and (b) FG-NCM92 layered oxide cathode materials.

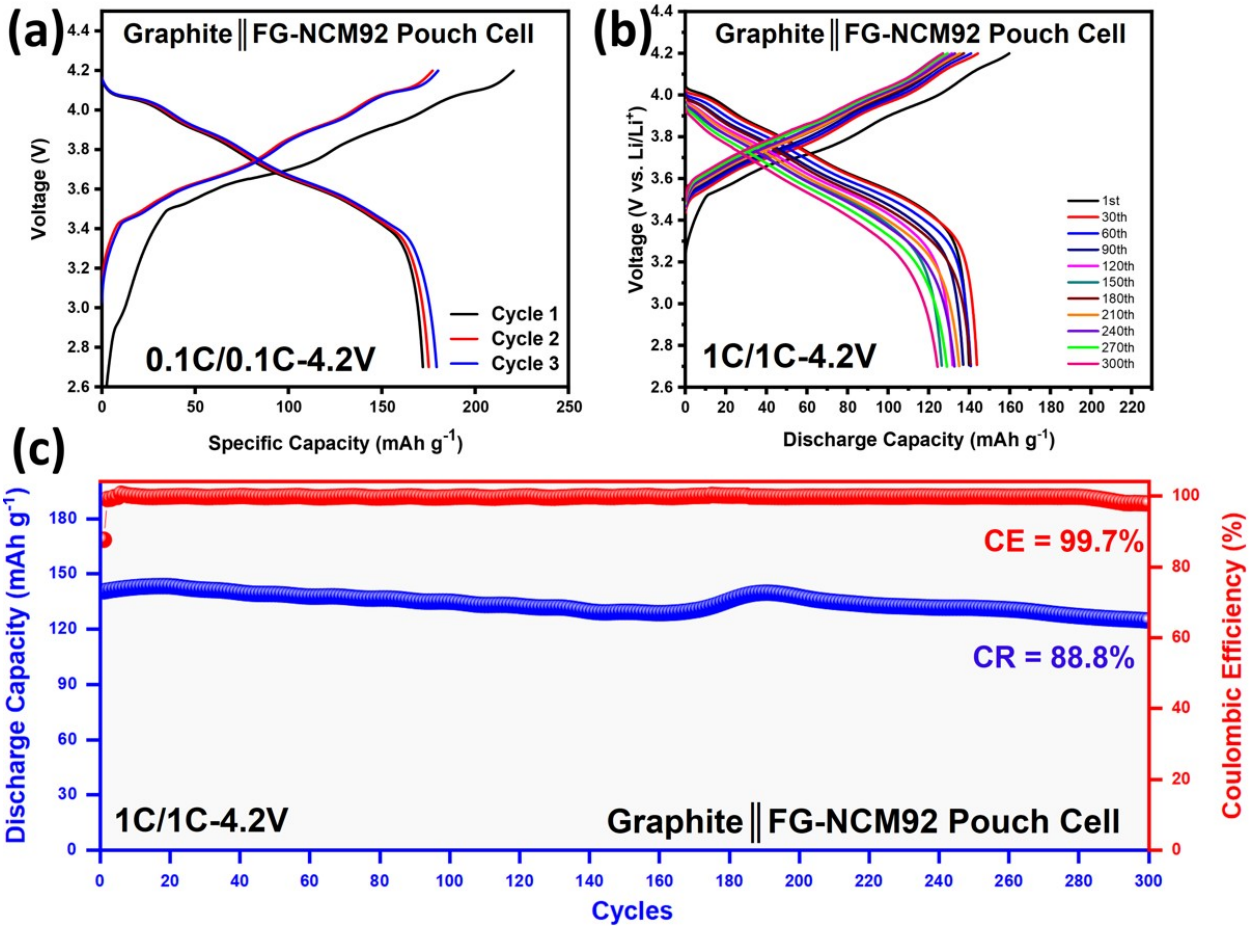

Fig. S12. The electrochemical performance of FG-NCM92//Graphite Pouch cells: (a). The charge and discharge profiles at 0.1C/0.1C, (b). The charge and discharge profiles at 1C/1C, (c). Long-term cycling performance of FG-NCM92//Graphite based on Pouch-type full-cells (Size: 3 × 5 cm^2).

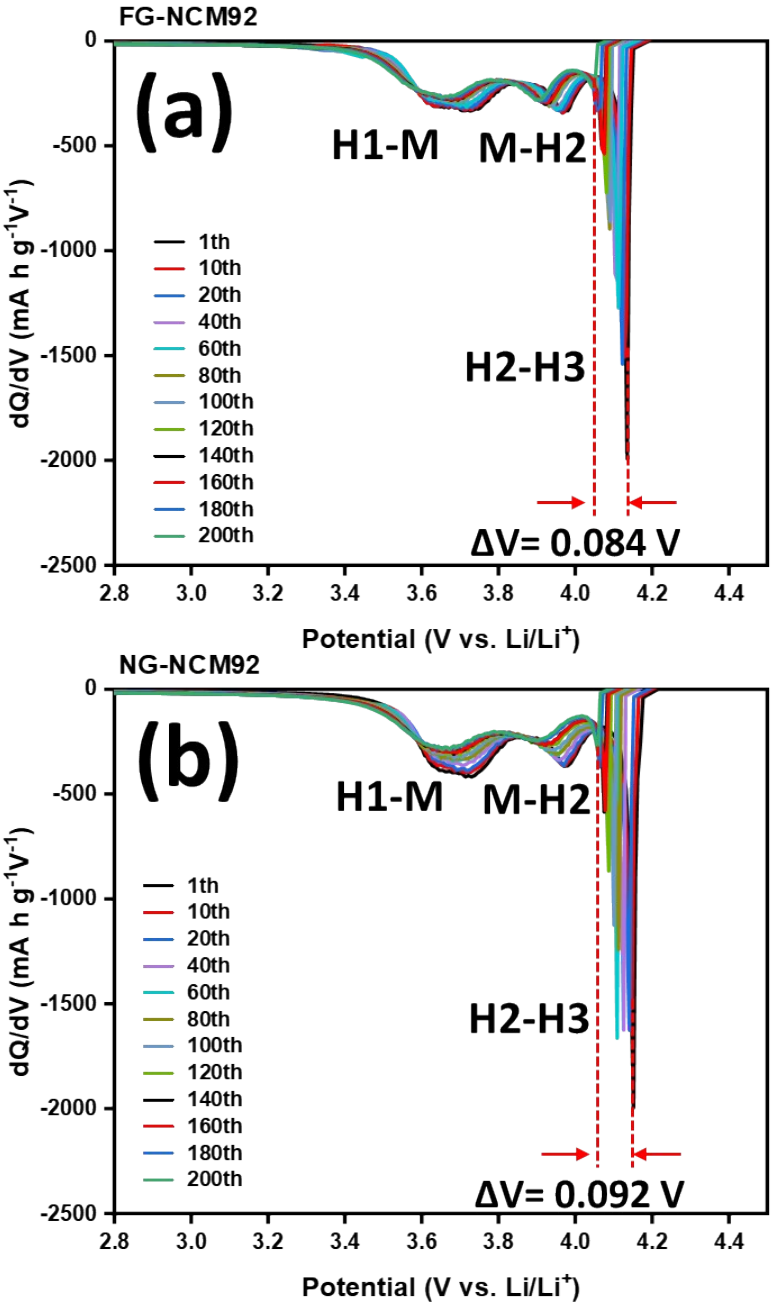

Fig. S13. Differential capacity (dQ/dV) curves of (a) FG-NCM92, and (b) NG-NCM92 cathodes at 1C/1C in the voltage window of 2.8–4.3 V at RT for 200 cycles.

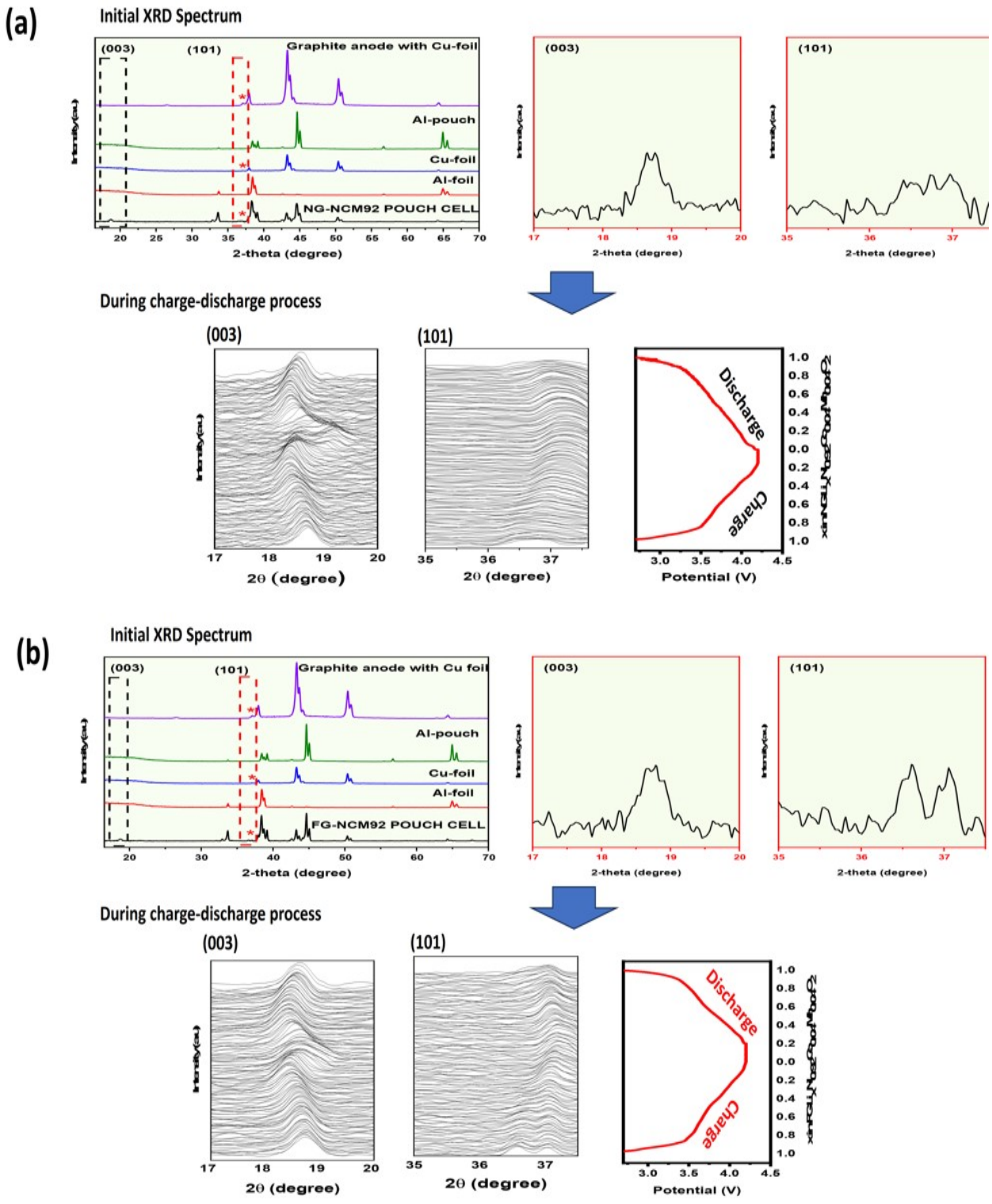

Fig. S14. Observed initial in-situ XRD pattern and XRD pattern at selected 2θ regions during initial cycles of charge/discharge process for (a) NG-NCM92, and (b) FG-NCM92 electrodes, respectively.

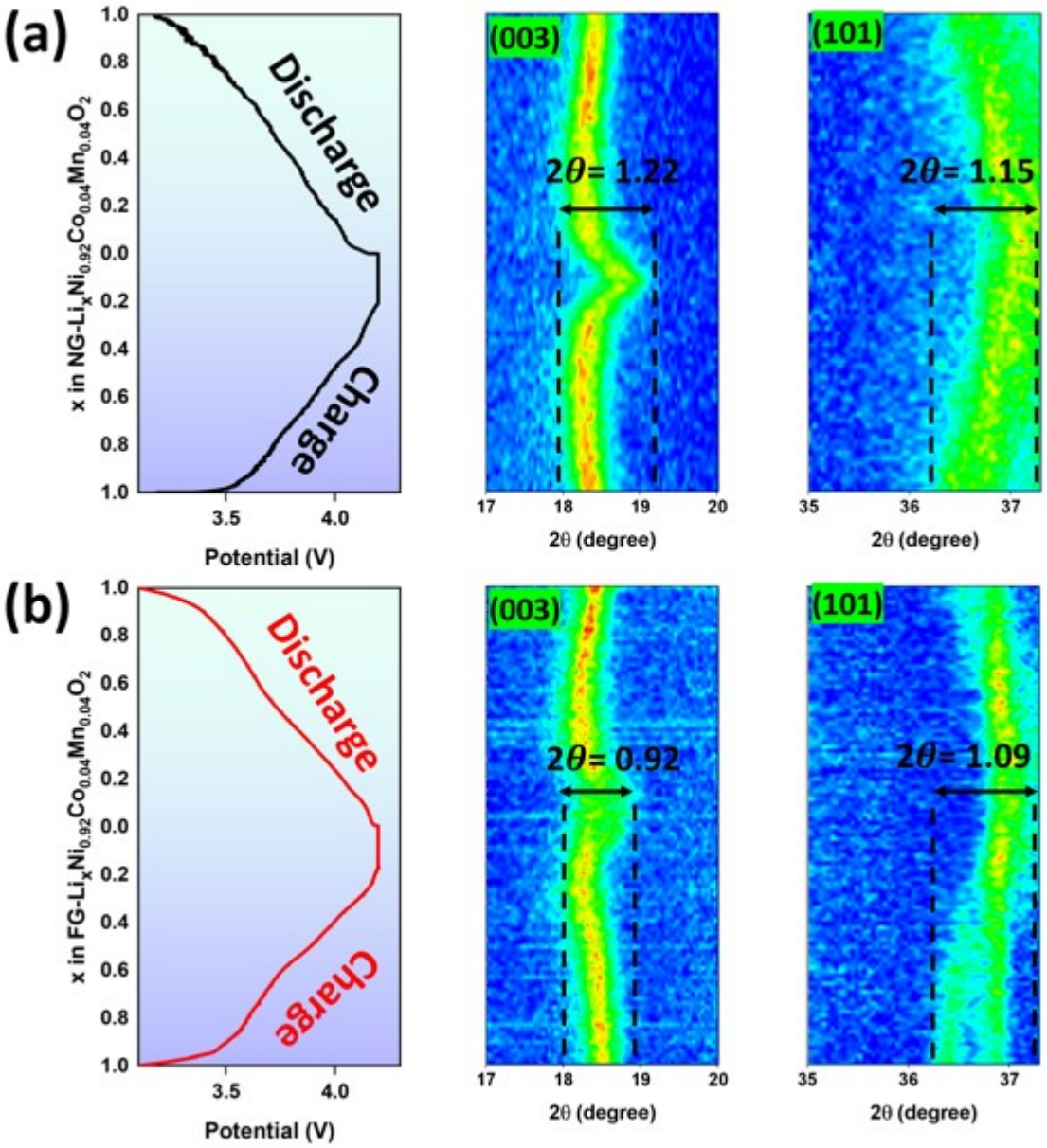

Fig. S15. In-situ XRD patterns at selected 2θ regions during second cycles for (a). NG-NCM92, (b). FG-NCM92 samples, respectively.

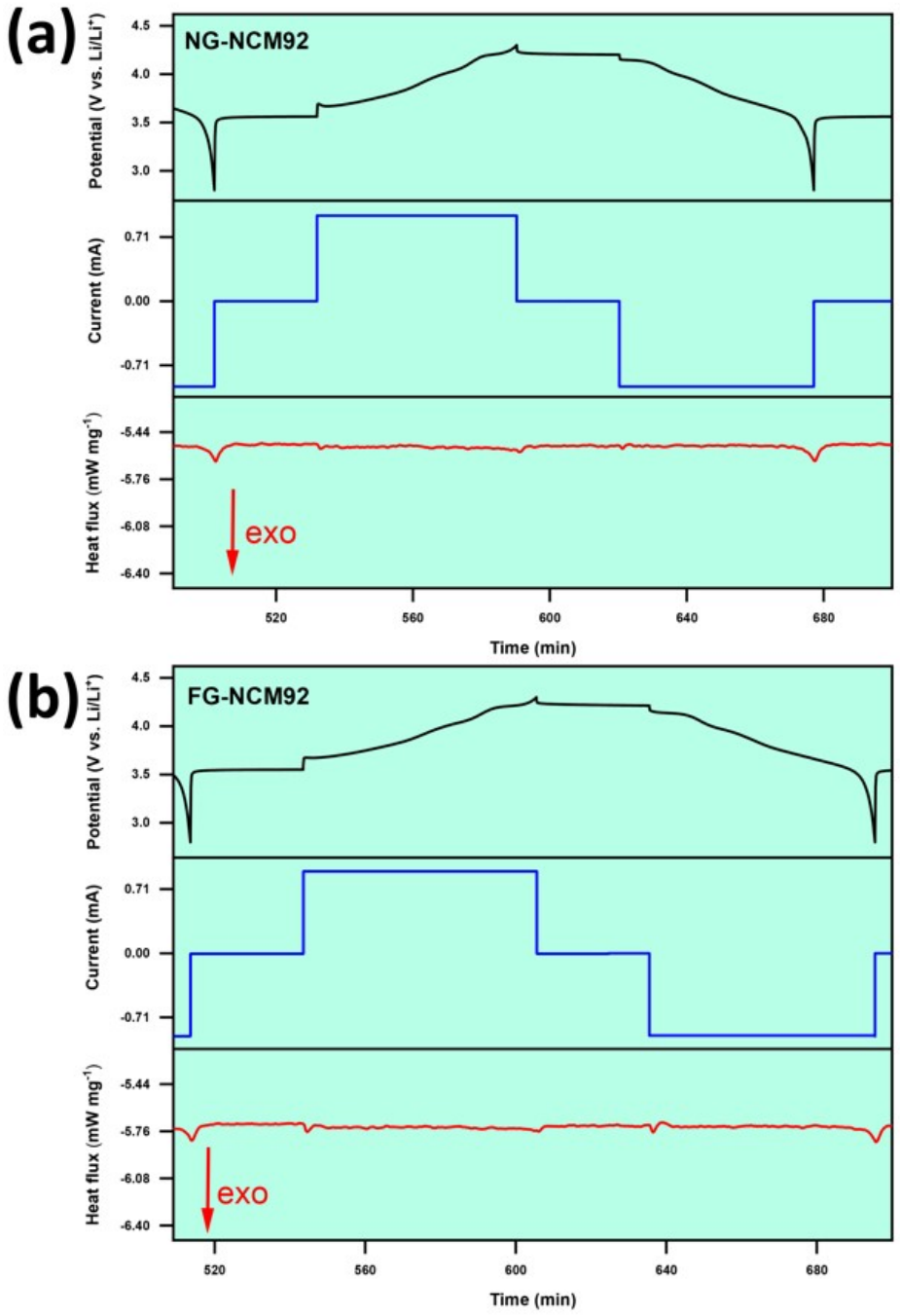

Fig. S16. Operando micro-calorimetry results for CR2032 coin cells containing: (a) NG-NCM92, and (b) FG-NCM92 electrodes at 1C/1C (in voltage window of 2.8–4.3 V (*vs.* Li/Li^+)) in isothermal conditions at 35˚C with heating rate of 0.5˚C min^{-1} (Potential (black line), current (blue line), and heat flux (red line).

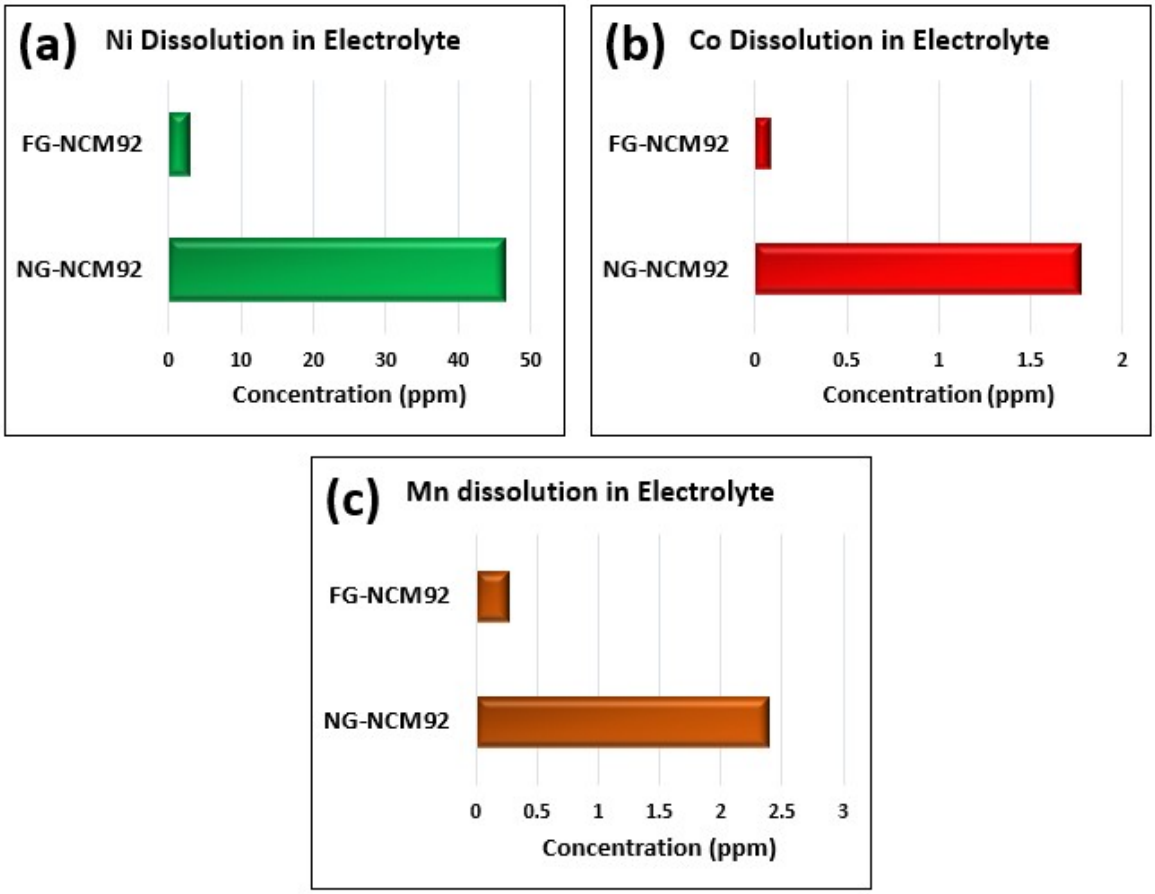

Fig. S17. The transition metal dissolution properties of NG-NCM92 and FG-NCM92 cathodes, which were measured by inductively coupled plasma mass spectrometry (ICP-MS): (a). Ni, (b). Co, (c). Mn.

Table S1. Rietveld refinement results of NG-NCM92 and FG-NCM92 layered oxide materials.

Sample	a (A)	c (A)	V (A^3)	c/a	FWHM of (003)	R = $I_{(003)}/I_{(104)}$	Crystallite size (nm)	R_{wp} [d] (%)	GoF[e]
NG-NCM92	2.874	14.193	101.544	4.938	0.162	1.78	49.62	3.66	1.84
FG-NCM92	2.873	14.195	101.451	4.942	0.156	1.82	51.46	3.92	2.07

Table S2. The in-situ XRD lattice parameters for NG-NCM92 and FG-NCM92 layered oxide materials during initial cycles.

	NG-NCM92			FG-NCM92		
	Lithiated state	Delithiated state	Δ_{max} (%)	Lithiated state	Delithiated state	Δ_{max} (%)
***c*-axis (Å)**	14.527	14.387	0.97	14.433	14.361	0.49
***a*-axis (Å)**	2.850	2.833	0.61	2.846	2.831	0.35
Unit-cell volume ($Å^3$)	101.50	100.11	1.37	100.74	99.873	0.86

Table S3. Fitting results of EIS spectra of NG-NCM92 and FG-NCM92 electrodes before cycling and after 200 cycles.

	Before Cycling		After 200 Cycles	
Sample	NG-NCM92	FG-NCM92	NG-NCM92	FG-NCM92
$R_b(\Omega)$	3.76	1.55	4.63	3.05
$R_{CEI}(\Omega)$	—	—	6.17	6.10
$R_{int}(\Omega)$	—	—	20.50	18.00
$R_{ct}(\Omega)$	138.50	118.50	610.00	581.80

Table S4. The Total Exothermic Heat Generation (Q_t) and heat reduction of the NG-NCM92//Li coin-type cell and FG-NCM92//Li coin-type during charge/discharge processes at 35 °C.

Total heat generation / Electrode	*Q_t (J g^{-1})		Heat reduction (%) *vs*. NG-NCM92	
	Charge	Discharge	Charge	Discharge
NG-NCM92	-18.94	-26.59	—	—
FG-NCM92	-17.57	-23.04	7.2	13.4

*A negative Q_t value indicates an exothermic heat release